Computers and Structures 92-93 (2012) 242–256

Contents lists available at SciVerse ScienceDirect

Computers and Structures

journal homepage: www.elsevier.com/locate/compstruc

Phantom-node method for shell models with arbitrary cracks

Thanh Chau-Dinh [a], Goangseup Zi [a,*], Phill-Seung Lee [b], Timon Rabczuk [c], Jeong-Hoon Song [d]

[a] Department of Civil, Environmental & Architectural Engineering, Korea University, 5 Ga 1, An-Am Dong, Sung-Buk Gu, Seoul 136-701, South Korea
[b] Division of Ocean Systems Engineering, Korea Advanced Institute of Science and Technology (KAIST), 291 Daehakro, Yu-Seong Gu, Daejeon 305-701, South Korea
[c] Institute of Structural Mechanics, Bauhaus University Weimar, Marienstr. 15, 99425 Weimar, Germany
[d] Civil and Environmental Engineering, University of South Carolina, 300 Main street, Columbia, SC 29208, United States

ARTICLE INFO

Article history:
Received 22 April 2011
Accepted 28 October 2011

Keywords:
Phantom-node method
MITC3 shell element
Cracked shells
J-integral
Stress intensity factors

ABSTRACT

A phantom-node method is developed for three-node shell elements to describe cracks. This method can treat arbitrary cracks independently of the mesh. The crack may cut elements completely or partially. Elements are overlapped on the position of the crack, and they are partially integrated to implement the discontinuous displacement across the crack. To consider the element containing a crack tip, a new kinematical relation between the overlapped elements is developed. There is no enrichment function for the discontinuous displacement field. Several numerical examples are presented to illustrate the proposed method.

1. Introduction

The analysis of cracked shells is important in many engineering applications such as pressurized aircraft fuselages, pipe lines, storage tanks and so on. However, research on fracture mechanics of shells is complex compared to continuum problems due to the combination of in-plane and out-of-plane loading. The research that has considered the shell fracture on in-plane tensile loading or on bending orthogonal to the crack only is not reasonable in many practical cases involving asymptotic out-of-plane loadings, especially pressurized thin shells [1,2]. Therefore, accurate calculations of fracture parameters play a significant role in examining failure or predicting fatigue of shells containing cracks. Because analytical solutions have been derived only for shells of simple geometry and boundary conditions, numerical methods have been developed to deal with practical shells with complicated shapes and boundaries.

A popular method to analyze shell structure is the finite element method (FEM) [3–6]. However, modeling crack growth imposes a challenge on the FEM that usually requires remeshing. Alternative methods have been developed to overcome the cumbersome nature of remeshing. Such methods as the meshfree method [7–9] or the extended finite element method (XFEM) [10–12] have successfully modeled problems of shell fracture. However, the incorporation of the assumed strain techniques such as the mixed interpolation of tensorial components (MITC) [13] or the enhanced assumed strain (EAS) technique [14] to circumvent locking phenomena, or the smoothed strain technique [15] to improve numerical accuracy are not straightforward in XFEM. The key idea of these techniques is to design separately assumed strain fields based on the continuous and compatible gradient of displacement fields. Consequently, the XFEM with the presence of discontinuous enrichments in the approximated displacement fields used to describe crack kinematics may not employ these additional techniques in a straightforward manner.

Recently, Hansbo and Hansbo [16] have proposed another approach by duplicating homologous nodes to build overlapping paired elements for representing crack kinematics instead of adding enrichments and degrees of freedom as in the XFEM. Because there are no additional degrees of freedom introduced, "mixed" terms of a stiffness matrix for standard and additional degrees of freedom are not needed compared to the XFEM and so conditioning is improved. Based on the full interpolation bases of the overlapping elements, the idea of Hansbo and Hansbo can straightforwardly integrate the enhanced techniques in shell elements, although it is equivalent to the XFEM as proven in [17]. This so-called phantom-node method has been implemented in the finite element framework in two dimensions [18,19], three dimensions [20,21], and thin shells based on discrete Kirchhoff theory [22–24].

In this paper, we present further developments of the phantom-node method for shells with through-the-thickness cracks normal to the midsurface. The shells are discretized by continuum mechanics based shell elements. These are three-node isotropic triangular elements with the MITC technique designed to attenuate the shear-locking phenomenon and to satisfy the requirement

* Corresponding author.
E-mail address: g-zi@korea.ac.kr (G. Zi).

0045-7949/$ - see front matter © 2011 Elsevier Ltd. All rights reserved.
doi:10.1016/j.compstruc.2011.10.021

of spatial isotropy [25,26]. In other words, this MITC3 shell element can strongly reduce the excess of stiffness characterizing the shear-locking problem and its stiffness matrix is independent of how the nodes are numbered. Moreover, kinematic constraints of overlapping paired elements for tip elements within which the tip of a crack is located are derived as an extension from the formulation given in [19] for two-dimensional tip elements. Hence, elements do not need to be completely cut by cracks, in contrast to [22–24].

A suitable domain form of the *J*-integral for cracked shells discretized by the MITC3 elements is formulated as a special case of the "equivalent domain integral" method for three-dimensional fracture problems [27]. For this derivation, the MITC3 element is treated similarly to a three-dimensional continuum element. Owing to the MITC technique, the formulation for the domain form of the *J*-integral can also handle thin shells. Similarly, a domain form of the interaction integral is derived to extract the mixed-mode stress intensity factors, each of which corresponds to in-plane and out-of-plane loadings. To demonstrate the performance of the method, some fracture problems of plane stress, plates and shells are solved and compared to analytical or semi-analytical solutions.

The paper is outlined as follows. In the following section we present formulations of the MITC3 shell element discretized for a cracked shell model in conjunction with the phantom-node method. Section 3 describes the discretized equilibrium equations. Calculation of the *J*-integral and the stress intensity factors using the domain form for shells is given in Section 4. Some numerical examples are solved in Section 5 and conclusions are drawn in Section 6.

2. Finite element discretization for a cracked shell model

We consider the finite element discretization of a shell model with an arbitrary through-the-thickness crack. Because of the crack, there are three types of finite elements, namely uncracked, cracked, and tip elements; note that the tip elements are partially cut by the crack. Details of the finite element formulation for each type of element are presented in the following sections.

2.1. Three-node isotropic triangular MITC shell elements for uncracked elements

An uncracked element, on which the displacement field is continuous, can be treated as the standard finite element method. In computational analysis of shells, approaches based on continuum mechanics based shell elements originated from the work of Ahmad et al. [28] are popular due to their simplicity of formulation and implementation in the finite element procedures [29]. Unfortunately, the displacement based elements are too stiff in bending-dominated shell problems when the thickness is small, leading to locking phenomena [25,30]. To alleviate the locking, there are many methods such as uniform reduced integration (URI) [31,32], selective reduced integration (SRI) [33,34], assumed natural strain (ANS) [35,36] or so-called mixed interpolation of tensorial components (MITC) [13,37], or enhanced assumed strain (EAS) [14,38], to name a few. Among these, the effectiveness of the MITC technique has been well studied [39] and the MITC shell elements have been mostly adopted in commercial finite element software.

In this paper, the uncracked part is discretized by the linear MITC3 element of Lee and Bathe [25]. Particularly, since the three-node element has flat geometry, it only suffers from shear locking. To ameliorate the shear locking and meet the requirement of spatial isotropy, the MITC technique here was designed such that the transverse shear strain variations corresponding to the three edge directions of the element are identical.

In the continuum mechanics based shell elements proposed by [28], the displacement approximation can be obtained by considering geometric approximation mapping of any point $\mathbf{x}$ of the shell in the global Cartesian coordinate system (x,y,z) into the natural coordinates (ξ,η,ζ) as defined in [40]

$$\mathbf{x}(\xi,\eta,\zeta)=\sum_{I=1}^{3}N_I(\xi,\eta)\mathbf{x}_I+\frac{\zeta}{2}\sum_{I=1}^{3}h_I N_I(\xi,\eta)\mathbf{V}_I^n \tag{1}$$

where $N_I(\xi,\eta)$ is the standard C^0 shape function corresponding to the surface ζ = constant; $\mathbf{x}_I$ is the nodal coordinates in the global Cartesian system; and h_I and $\mathbf{V}_I^n$ denote the shell thickness and the director vector, respectively. The subscript I indicates the values at node I.

The displacement approximation $\mathbf{u}$ of the element is then given by

$$\mathbf{u}(\xi,\eta,\zeta)=\sum_{I=1}^{3}N_I(\xi,\eta)\mathbf{u}_I+\frac{\zeta}{2}\sum_{I=1}^{3}h_I N_I(\xi,\eta)(-\mathbf{V}_I^2\alpha_I+\mathbf{V}_I^1\beta_I) \tag{2}$$

wherein, $\mathbf{V}_I^1$ and $\mathbf{V}_I^2$ are unit vectors orthogonal to $\mathbf{V}_I^n$ and each other to create a nodal coordinate system at node I, see Fig. 1; $\mathbf{u}_I=\{u_I,v_I,w_I\}^T$ is the translational displacements in the global Cartesian coordinate system, and (α_I,β_I) are the rotational displacements of the director vector $\mathbf{V}_I^n$ about $\mathbf{V}_I^1$ and $\mathbf{V}_I^2$, respectively, in the nodal coordinate system.

The purely displacement-based three-node shell elements suffer from a severe "shear locking" phenomenon as the shell thickness decreases. To circumvent the shear locking, the covariant transverse shear strains in the MITC3 element are separately interpolated from values of the covariant transverse shear strains evaluated at "tying points" which are the center of the isotropic element edges as shown in Fig. 2. To satisfy the isotropic property of the transverse shear strain fields, their interpolations were constructed by [25] as follows

$$\tilde{\varepsilon}_{\xi\zeta}^{MITC3}=\tilde{\varepsilon}_{\xi\zeta}^{(1)}+c\eta \tag{3a}$$

$$\tilde{\varepsilon}_{\eta\zeta}^{MITC3}=\tilde{\varepsilon}_{\eta\zeta}^{(2)}-c\xi \tag{3b}$$

in which,

$$c=\tilde{\varepsilon}_{\eta\zeta}^{(2)}-\tilde{\varepsilon}_{\xi\zeta}^{(1)}-\tilde{\varepsilon}_{\eta\zeta}^{(3)}+\tilde{\varepsilon}_{\xi\zeta}^{(3)} \tag{4}$$

and the covariant strain components are derived as

$$\tilde{\varepsilon}_{ij}=\frac{1}{2}(\mathbf{g}_i\cdot\mathbf{u}_{,j}+\mathbf{g}_j\cdot\mathbf{u}_{,i}) \tag{5}$$

where

$$\mathbf{g}_i=\frac{\partial\mathbf{x}}{\partial\xi_i};\quad \mathbf{u}_{,i}=\frac{\partial\mathbf{u}}{\partial\xi_i}\quad \text{with } \xi_1=\xi,\quad \xi_2=\eta,\quad \xi_3=\zeta \tag{6}$$

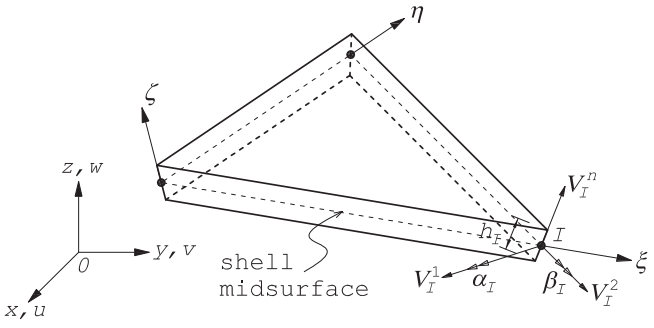

Fig. 1. Three-node shell finite element.

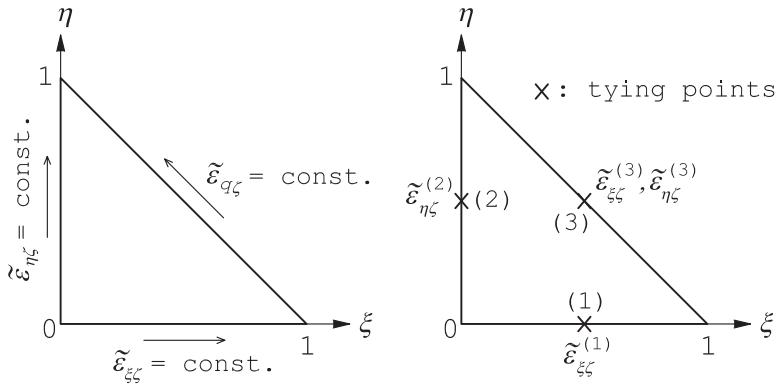

Fig. 2. Constant transverse shear strain along edges and positions of tying points.

Next, we use the relationships between the components of the covariant strain tensor $\tilde{\varepsilon}_{ij}$ and those of the global Cartesian strain tensor ε_{mn} [40]

$$\tilde{\varepsilon}_{ij}\mathbf{g}^i \otimes \mathbf{g}^j = \varepsilon_{mn}\mathbf{e}_m \otimes \mathbf{e}_n \tag{7}$$

in which $\mathbf{g}^i$ are the contravariant base vectors and satisfy $\mathbf{g}_i \cdot \mathbf{g}^j = \delta_i^j$, the (mixed) Kronecker delta, and $\mathbf{e}_m$ are the unit base vectors defined in the global Cartesian coordinate system, to transform the in-plane and transverse strain components respectively given in equations (5) and (3) into those measured in the global Cartesian coordinate system. The strain–displacement matrix **B** can then be formulated.

2.2. Overlapping paired elements for cracked elements

In a cracked element, which is completely cut by a crack, the displacement field is discontinuous across the crack but independently continuous on each part of the element. Hence, the displacement field can be superimposed by two separate displacement fields, each of which is continuous on its own part of the element as illustrated in Fig. 3. This technique is given in the paper of Hansbo and Hansbo [16]. While it has been proved to be equivalent to the XFEM [17], this approximation of the displacement field for the cracked element exhibits more advantages since there are no discontinuous enrichments required. The gradient of the displacement field is continuous on each part of the cracked element. The shell formulations can then be simply implemented on each part of the cracked element as a pair of overlapping standard MITC3 elements.

Let a cracked element Ω_e be divided into two complementary parts, Ω_e^+ and Ω_e^-, by a crack. The displacement field in the cracked element can be described as

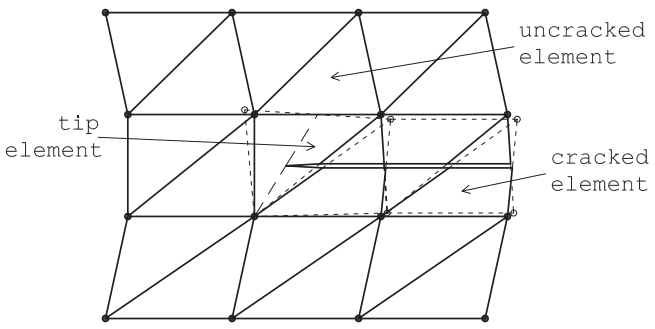

Fig. 3. Displacement jump described by the phantom-node method. Solid circles are physical nodes; empty circles are phantom nodes.

$$\mathbf{u}_{cr} = \begin{cases} \mathbf{u}^+ & \text{in } \Omega_e^+ \\ \mathbf{u}^- & \text{in } \Omega_e^- \end{cases} \tag{8}$$

To use the standard approximation of the displacement field on each part of the cracked element, the real parts Ω_e^+ and Ω_e^- are extended to their opposite sides as Ω_e^{P-} and Ω_e^{P+}, respectively, by additionally introducing the local duplication of homologous nodes called phantom-nodes, as shown in Fig. 4. These nodes have the same director vectors as the real nodes. As a result, the continuous displacement field on each part of the cracked element can be approximated similarly to that of the continuum mechanics based shell element

$$\mathbf{u}_{cr}(\xi,\eta,\zeta) = \begin{cases} \sum_{K=1}^{3} N_K(\xi,\eta)\mathbf{u}_K + \frac{\zeta}{2}\sum_{K=1}^{3} h_K N_K(\xi,\eta)(-\mathbf{V}_K^2\alpha_K + \mathbf{V}_K^1\beta_K) & \text{in } \Omega_e^+ \\ \sum_{L=1}^{3} N_L(\xi,\eta)\mathbf{u}_L + \frac{\zeta}{2}\sum_{L=1}^{3} h_L N_L(\xi,\eta)(-\mathbf{V}_L^2\alpha_L + \mathbf{V}_L^1\beta_L) & \text{in } \Omega_e^- \end{cases} \tag{9}$$

where $K \in \{1,2^*,3^*\}$ and $L \in \{1^*,2,3\}$ are nodes belonging to $\Omega_e^+ \cup \Omega_e^{P-}$ and $\Omega_e^- \cup \Omega_e^{P+}$, respectively.

The MITC technique, given in Eqs. (3) and (4), is now applied straightforwardly to the continuous displacement fields in Eq. (9) of the overlapping paired elements of which the domains are $\left(\Omega_e^+ \cup \Omega_e^{P-}\right)$ and $\left(\Omega_e^- \cup \Omega_e^{P+}\right)$. Similarly to the formulations for the MITC3 element in Section 2.1, the corresponding strain–displacement matrices can be obtained for the displacement fields in Eq. (9) realized only on the real parts, i.e. Ω_e^+ and Ω_e^-.

2.3. Constrained overlapping paired elements for tip elements

The displacement field in tip elements jumps across the partially intersected crack but does not jump at the tip as shown in Fig. 5. To improve the accuracy of the displacement field, the classical XFEM uses branch enrichments which are basic functions of the asymptotic displacement fields near the crack tip [41,42], while the standard FEM implements the crack tip singularity by using the quarter point distortion [3]. However, the analytical solution is known only in a few cases; therefore, the branch enrichments that we do not have, only add complexity but do not necessarily improve the results in the XFEM.

In fact, Dolbow et al. [42] mentioned that the enriched approximation may cause a shear locking which reduces the accuracy of the moment intensity factor in the XFEM applied to shell problems; for an infinite plate with a central crack subjected to a far-field moment, the XFEM was even worse than the standard FEM as the thickness was very thin. In the FEM, some authors [4,6] have shown that fracture behaviors of shell problems can be analyzed

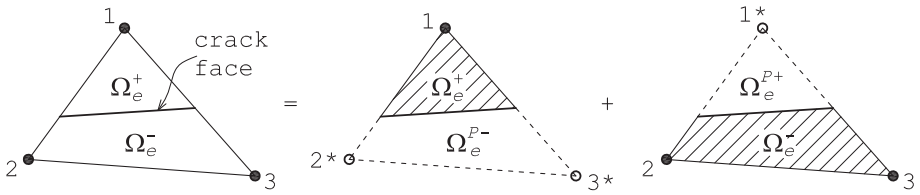

Fig. 4. Additional phantom nodes and phantom domains for cracked elements.

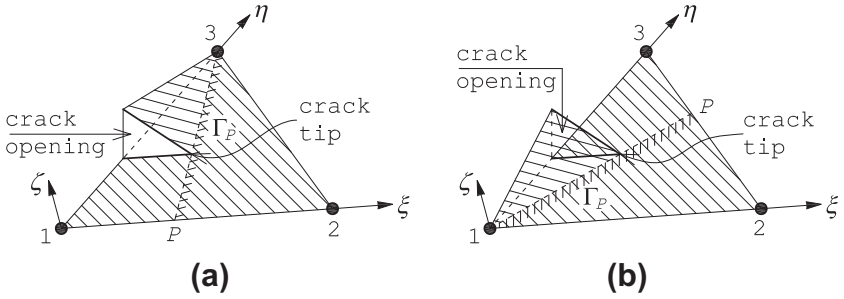

Fig. 5. Two possibilities of discontinuous displacement field (hatched area) with crack opening in a tip element.

with good accuracy without using the singular elements. This means that the branch enrichments or the singular elements are not always necessary. Moreover, branch enrichments are difficult to incorporate in the phantom-node method.

In another approach, Zi and Belytschko [43] managed to satisfy the condition by using the step enrichment only and a different shape function for the enriched field of the displacement approximation, which results in the crack-opening displacement vanishing at edge Γ_P, see Fig. 5. By omitting the branch enrichments, numerical computation is less costly since it avoids the problems related to blending and integrating the singularity and the non-polynomial terms. This approach was extended to derive a simple tip element for the phantom-node method used in two-dimensional problems [19].

Based on the work of Rabczuk et al. [19], we now develop overlapping paired elements for a three-node triangular shell element containing a tip. Assume that a partial crack cuts edge $\overline{13}$ (in natural coordinates) of the tip element. There are two possibilities of the discontinuous displacement fields in the tip element as illustrated in Fig. 5. Consider the displacement field required in Fig. 5a. To provide a set of full interpolation bases for the displacement field of the small triangle, phantom nodes 1^* and 2^* are added at the position of nodes 1 and 2, respectively, to create a completely new three-node triangular shell element. The tip element is now decomposed into two elements $\triangle 123$ and $\triangle 1^*2^*3$, which share node 3 (see Fig. 6a). As a result, for each overlapping paired element the formulations of the MITC3 element can be implemented straightforwardly similarly to that for cracked elements.

Additionally, since the crack-opening displacement at the tip vanishes, the displacement approximations of the overlapping paired elements must be identical along the Γ_P edge, as demonstrated in Fig. 6. To satisfy this kinematical condition, the nodal displacements of the overlapping paired elements must be constrained. For the case given in Fig. 6a, using the similarity of triangles $\triangle 1P1^*$ and $\triangle 2P2^*$, the displacements of phantom node 2^* are constrained as

$$\xi_P(\mathbf{q}_2-\mathbf{q}_{2^*})=(1-\xi_P)(\mathbf{q}_{1^*}-\mathbf{q}_1)$$
$$\Rightarrow\ \mathbf{q}_{2^*}=\frac{1-\xi_P}{\xi_P}\mathbf{q}_1+\mathbf{q}_2-\frac{1-\xi_P}{\xi_P}\mathbf{q}_{1^*} \tag{10}$$

here, $\mathbf{q}_i=\{\mathbf{u}_i^T,\alpha_i,\beta_i\}^T$ is the nodal translational and rotational displacements.

Or, the nodal displacements of the overlapping paired element are constrained in the matrix form as

$$\begin{Bmatrix}\mathbf{q}_{1^*}\\ \mathbf{q}_{2^*}\\ \mathbf{q}_3\end{Bmatrix}=\mathbf{T}^*\mathbf{q}_e^{tip-} \tag{11}$$

with

$$\mathbf{T}^*=\begin{bmatrix}\mathbf{0}&\mathbf{0}&\mathbf{0}&\mathbf{I}\\ \frac{1-\xi_P}{\xi_P}\mathbf{I}&\mathbf{I}&\mathbf{0}&-\frac{1-\xi_P}{\xi_P}\mathbf{I}\\ \mathbf{0}&\mathbf{0}&\mathbf{I}&\mathbf{0}\end{bmatrix}\quad\text{and}\quad\mathbf{q}_e^{tip-}=\begin{Bmatrix}\mathbf{q}_1\\ \mathbf{q}_2\\ \mathbf{q}_3\\ \mathbf{q}_{1^*}\end{Bmatrix} \tag{12}$$

For the other case in Fig. 6b in which node 1 is shared, the kinematical constraint of phantom node 2^* gives

$$\xi_P(\mathbf{q}_2-\mathbf{q}_{2^*})=(1-\xi_P)(\mathbf{q}_{3^*}-\mathbf{q}_3)$$
$$\Rightarrow\ \mathbf{q}_{2^*}=\mathbf{q}_2+\frac{1-\xi_P}{\xi_P}\mathbf{q}_3-\frac{1-\xi_P}{\xi_P}\mathbf{q}_{3^*} \tag{13}$$

In the matrix form, the relationship between the nodal displacements of the overlapping paired elements in Fig. 6b is

$$\begin{Bmatrix}\mathbf{q}_1\\ \mathbf{q}_{2^*}\\ \mathbf{q}_{3^*}\end{Bmatrix}=\mathbf{T}^*\mathbf{q}_e^{tip-} \tag{14}$$

with

$$\mathbf{T}^*=\begin{bmatrix}\mathbf{I}&\mathbf{0}&\mathbf{0}&\mathbf{0}\\ \mathbf{0}&\mathbf{I}&\frac{1-\xi_P}{\xi_P}\mathbf{I}&-\frac{1-\xi_P}{\xi_P}\mathbf{I}\\ \mathbf{0}&\mathbf{0}&\mathbf{0}&\mathbf{I}\end{bmatrix}\quad\text{and}\quad\mathbf{q}_e^{tip-}=\begin{Bmatrix}\mathbf{q}_1\\ \mathbf{q}_2\\ \mathbf{q}_3\\ \mathbf{q}_{3^*}\end{Bmatrix} \tag{15}$$

Similarly, we can obtain the constrained matrix $\mathbf{T}^*$ for the other cases where the partial crack cuts edges $\overline{12}$ or $\overline{23}$ of the tip shell element.

3. Equilibrium equations and numerical integration

3.1. Discretized equilibrium equations

A shell model Ω containing a crack Γ_{cr} is given. The model is constrained on the necessary boundary Γ_u and sustains an external

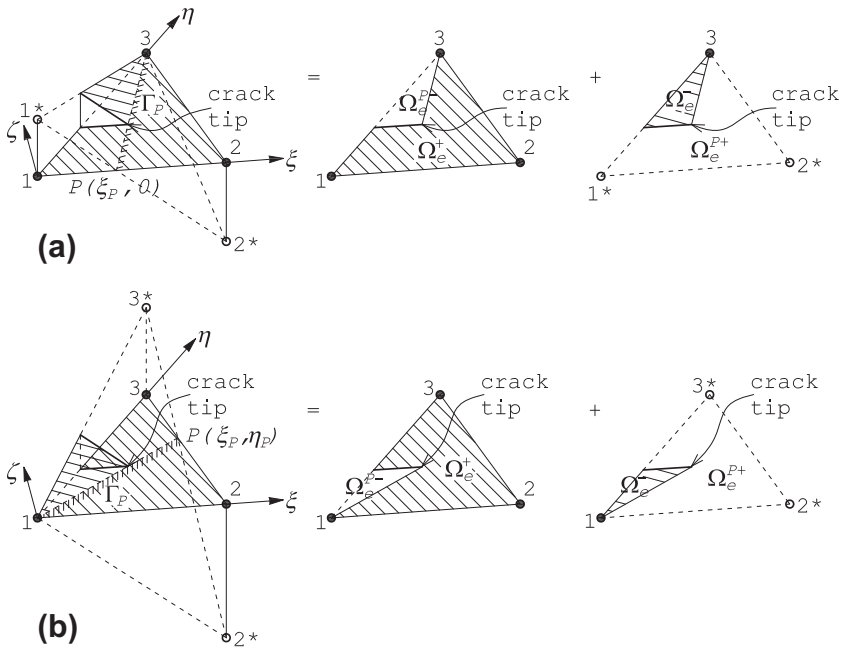

Fig. 6. Additional phantom nodes (empty circle) determined by the kinematical constraints for the two possibilities of displacement field given in Fig. 5.

load of traction $\boldsymbol{\tau}_0$ on the natural boundary, Γ_t. Note that $\Gamma_u \cup \Gamma_t = \Omega$ and $\Gamma_u \cap \Gamma_t = \emptyset$. It is assumed that the crack surface is free of traction and the material is linear isotropic elasticity.

As the conventional finite element procedure, the discretized equations of equilibrium can be obtained as

$$\mathbf{f}^{int} = \mathbf{K}\mathbf{q} = \mathbf{f}^{ext} \tag{16}$$

where $\mathbf{f}^{int}$ and $\mathbf{f}^{ext}$ are the discrete internal and external forces, respectively, $\mathbf{K}$ is the stiffness matrix, and $\mathbf{q}$ are the generalized nodal displacements, including all physical and phantom nodes. The expressions for $\mathbf{f}^{int}$ and $\mathbf{f}^{ext}$ are given by

$$\begin{aligned}\mathbf{f}^{int} = &\sum_{\substack{\text{uncracked}\\ \text{elements}}} \int_{\Omega_e} \mathbf{B}^T\mathbf{C}\mathbf{B}\,d\Omega\mathbf{q}_e \\ &+ \sum_{\substack{\text{cracked}\\ \text{elements}}} \left(\int_{\Omega_e^+} \mathbf{B}^T\mathbf{C}\mathbf{B}\,d\Omega\mathbf{q}_e^{cr+} + \int_{\Omega_e^-} \mathbf{B}^T\mathbf{C}\mathbf{B}\,d\Omega\mathbf{q}_e^{cr-} \right) \\ &+ \sum_{\substack{\text{tip}\\ \text{elements}}} \left(\int_{\Omega_e^+} \mathbf{B}^T\mathbf{C}\mathbf{B}\,d\Omega\mathbf{q}_e^{tip+} + \int_{\Omega_e^-} \mathbf{T}^{*T}\mathbf{B}^T\mathbf{C}\mathbf{B}\mathbf{T}^* d\Omega\mathbf{q}_e^{tip-} \right)\end{aligned} \tag{17}$$

$$\mathbf{f}^{ext} = \sum_{\substack{\text{all}\\ \text{elements}}} \int_{\Gamma_e} \mathbf{N}^T\boldsymbol{\tau}_0\,d\Gamma \tag{18}$$

where $\mathbf{B}$ is the strain–displacement matrix of the MITC3 shell element established on physical nodes for the uncracked elements and nodes belonging to the overlapped paired elements $\Omega_e^+ \cup \Omega_e^{P-}$ or $\Omega_e^- \cup \Omega_e^{P+}$ for the cracked or tip elements; $\mathbf{q}_e$ is the nodal displacements of an uncracked element; $\mathbf{q}_e^{cr+}$ and $\mathbf{q}_e^{cr-}$ are the nodal displacements of the overlapped paired elements $\Omega_e^+ \cup \Omega_e^{P-}$ and $\Omega_e^- \cup \Omega_e^{P+}$, respectively, for the cracked elements; $\mathbf{q}_e^{tip+}$ and $\mathbf{q}_e^{tip-}$ are the displacements of all physical nodes and physical nodes plus a phantom node, respectively, of the overlapping paired tip elements; $\mathbf{T}^*$ is the constrained matrix similar to equations (12) or (15); $\mathbf{C}$ is the constitutive matrix representing the linear elastic stress–strain law in the Cartesian coordinates and given in [40]

$$\mathbf{C} = \mathbf{Q}^T \left(\frac{E}{1-\nu^2} \begin{bmatrix} 1 & \nu & 0 & 0 & 0 & 0 \\ & 1 & 0 & 0 & 0 & 0 \\ & & 0 & 0 & 0 & 0 \\ & & & \frac{1-\nu}{2} & 0 & 0 \\ & & \text{sym.} & & k\frac{1-\nu}{2} & 0 \\ & & & & & k\frac{1-\nu}{2} \end{bmatrix} \right) \mathbf{Q} \tag{19}$$

in which, E, ν, and k are the Young's modulus, the Poison's ratio, and the shear correction factor, respectively; $\mathbf{Q}$ is a matrix that transforms the stress–strain law from an Cartesian shell-aligned coordinate system to the global Cartesian coordinate system.

3.2. Numerical integration

For elements not cut by a crack, the standard Gaussian method with (3×2) quadrature points, i.e. 3 in the in-plane and 2 in the thickness direction, is applied to numerically evaluate definite integrals.

To obtain a description of discontinuity by overlapping paired elements, the definite integrals need to be integrated on their own real parts only. To this end, the definite integration can be computed by subdividing domains into quadrature subtriangulars [41] or using numerical integration techniques for arbitrary polygonal domains. In this paper, for simplicity we subdivide the real parts into subtriangular domains aligned with the crack. The standard Gaussian quadratures and weights are modified by mapping into the subtriangular domains as described in [41] (see Fig. 7).

4. Calculation of fracture parameters

In this section, we describe the domain form of the path-independent J-integral for continuum mechanics based shell models. Additionally, the formulations for extraction of mixed-mode stress intensity factors in shell models with an arbitrary crack are derived based on the domain form of the interaction integral.

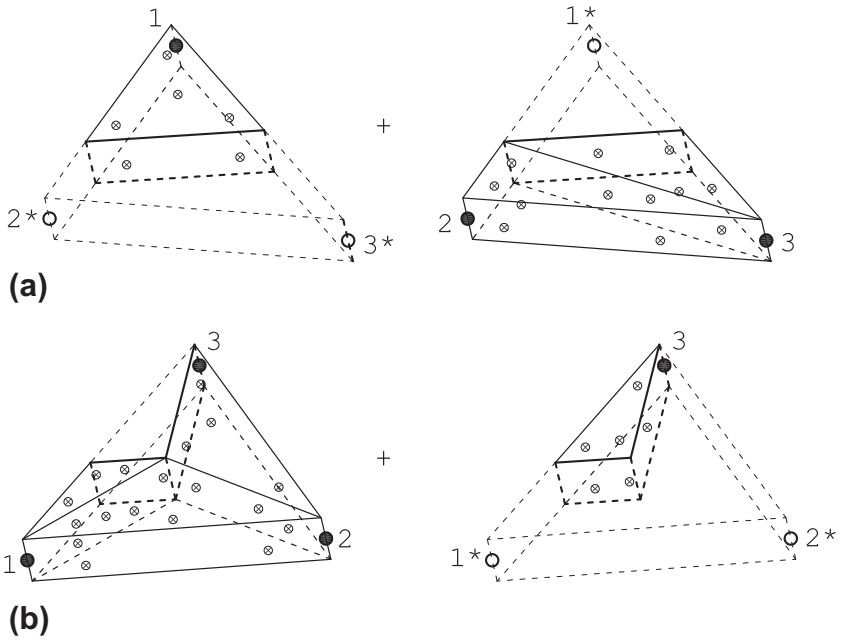

Fig. 7. Sub-triangles for real parts of elements containing discontinuity: (a) crack element; (b) tip element. Each sub-triangle has (3 × 2) Gaussian quadrature points (cross circles).

4.1. Domain form for J-integral calculation

Let us consider a through-the-thickness crack with the crack front normal to the mid-surface of the shell model as shown in Fig. 8. The *J*-integral is redefined as [27]

$$fJ = \int_S \left(\sigma_{ij}\frac{\partial u_i}{\partial x_1} - W\delta_{1j}\right) n_j q \mathrm{d}S \tag{20}$$

in which, $W = \frac{1}{2}\sigma_{ij}\varepsilon_{ij}$ is the strain energy density, σ_{ij} is the stress, ε_{ij} is the strain, u_i is the displacement, n_j is a component of the unit normal vector to the surface S of a volume V surrounding the crack front, δ_{1j} is the Kronecker delta, q is an arbitrary but continuous function which is equal to zero on A and non-zero on A_ε, and f is the area under the q function curve along the crack front, see Fig. 8.

Here, the value of J, which is equivalent to the energy release rate G in the frame of linear elastic fracture mechanics (LEFM), is computed in the direction x_1 of a local crack front coordinate system (x_1,x_2,x_3) at the tip.

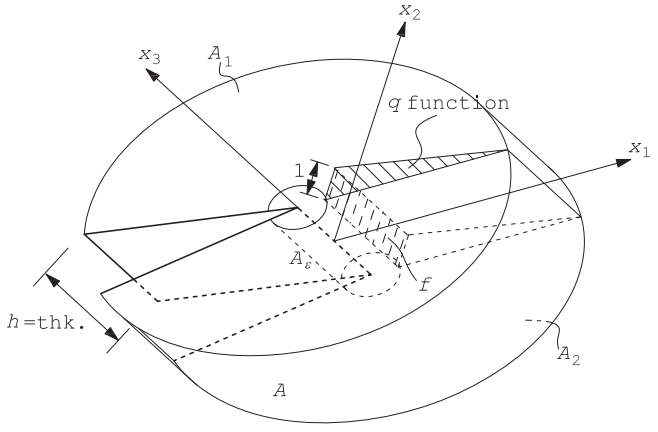

Fig. 8. Definition of J-domain, function q, and local coordinates at the tip of a crack in a shell.

Applying the divergence theorem to Eq. (20), we obtain the following domain form of *J*-integral in the case of LEFM

$$fJ = \int_V \left(\sigma_{ij}\frac{\partial u_i}{\partial x_1} - W\delta_{1j}\right)\frac{\partial q}{\partial x_j}\mathrm{d}V - \int_{A_1+A_2}\left(\sigma_{ij}\frac{\partial u_i}{\partial x_1} - W\delta_{1j}\right) n_j q \mathrm{d}S \tag{21}$$

For shell models discretized by the continuum mechanics based MITC3 elements, the domain form can be considered as a cylinder containing a crack front through the tip and normal to the midsurface. The cylinder is limited by the upper and lower faces, A_1 and A_2 of the shells. The local coordinates (x_1,x_2,x_3) are constructed by x_1 normal to the crack front or tangent to the midsurface, x_3 normal to the midsurface and x_2 orthogonal to $x_1$and x_3 following the right-handed rule (Fig. 8). We simply assume that A_1 and A_2 are equal and orthogonal to the crack front. Then,

$$n_1 = n_2 = 0, \quad n_3 = 1 \quad \text{on} \quad A_1$$
$$n_1 = n_2 = 0, \quad n_3 = -1 \quad \text{on} \quad A_2$$

and the q function is taken to be constant through the shell thickness, i.e. $f = h$, and equal to 1 on A_ε. Eq. (21) can be rewritten as

$$hJ = \int_V \left(\sigma_{ij}\frac{\partial u_i}{\partial x_1} - \frac{1}{2}\sigma_{ij}\varepsilon_{ij}\delta_{1j}\right)\frac{\partial q}{\partial x_j}\mathrm{d}V - \int_{A_1+A_2}\sigma_{i3}\frac{\partial u_i}{\partial x_1} n_3 q \mathrm{d}S \tag{22}$$

In Eq. (22), the stress, strain, and derivatives of displacements with respect to the local coordinate system (x_1,x_2,x_3) at the tip can be obtained by transforming those that are post-processing values of a finite element solution to the global Cartesian coordinate system (x,y,z) [27,40].

The last term of Eq. (22) is calculated using the integration points $\zeta = \pm 1/\sqrt{3}$ through the shell thickness as suggested in [27] as follows

$$hJ = \int_V \left(\sigma_{ij}\frac{\partial u_i}{\partial x_1} - \frac{1}{2}\sigma_{ij}\varepsilon_{ij}\delta_{1j}\right)\frac{\partial q}{\partial x_j}\mathrm{d}V - \sqrt{3} \times \int_{A_1}\left[F(\zeta = \frac{1}{\sqrt{3}}) - F\left(\zeta = \frac{-1}{\sqrt{3}}\right)\right] q \mathrm{d}S \tag{23}$$

with $F = \sigma_{i3}(\partial u_i/\partial x_1)$.

For finite element implementation, the domain V is a set of elements which has at least one node in and one node out of a circular cylinder with the central axis being the crack front and radius r_d. In this paper, the value of $r_d = 2.5h_{avg}$ will be used, wherein h_{avg} is the mean value of the square-roots of the cracked elements' areas [41].

The q function evaluated inside any element can be interpolated by means of finite element shape functions as

$$q = \sum_{I=1}^{3} N_I(\xi,\eta) q_I \tag{24}$$

in which $N_I(\xi,\eta)$ is the standard C^0 shape function, and q_I is the nodal value of function q, which is equal to 1 if node I is inside or equal to 0 if I is outside the circular cylinder.

4.2. Extraction of mixed-mode stress intensity factors

In LEFM, the stress intensity factors (SIFs) in shell models under combined in-plane and out-of-plane loadings are defined as a superposition of the plane stress and plate theory fields. The SIFs associated with each of the loadings in Fig. 9 have been thoroughly discussed in [2] and are briefly described as follows.

- Membrane loadings
  - Symmetric membrane loading: $K_I = \lim_{r\to 0}\sqrt{2\pi r}\sigma_{\theta\theta}(r,0)$
  - Antisymmetric membrane loading: $K_{II} = \lim_{r\to 0}\sqrt{2\pi r}\sigma_{r\theta}(r,0)$
- Kirchhoff theory's bending loadings
  - Symmetric loading (bending): $k_1 = \lim_{r\to 0}\sqrt{2r}\sigma_{\theta\theta}\left(r,0,\frac{h}{2}\right)$
  - Antisymmetric loading (twisting): $k_2 = \lim_{r\to 0}\frac{3+\nu}{1+\nu}\sqrt{2r}\sigma_{r\theta}\left(r,0,\frac{h}{2}\right)$
- Reissner theory's bending loadings
  - Symmetric loading (bending): $K_1 = \lim_{r\to 0}\sqrt{2r}\sigma_{\theta\theta}\left(r,0,\frac{h}{2}\right)$
  - Antisymmetric loading (twisting): $K_2 = \lim_{r\to 0}\sqrt{2r}\sigma_{r\theta}\left(r,0,\frac{h}{2}\right)$
  - Antisymmetric loading (bending): $K_3 = \lim_{r\to 0}\sqrt{2r}\sigma_{\theta 3}(r,0,0)$

where (r,θ) are the polar coordinates at a crack tip.

The relationship between the J-integral value and the SIFs in the cases of mixed-mode loadings is given as [2]

$$J = G = \frac{1}{E}\left(K_I^2 + K_{II}^2\right) + \frac{\pi}{3E}\left(\frac{1+\nu}{3+\nu}\right)\left(k_1^2 + k_2^2\right) \quad \text{for Kirchhoff theory} \tag{25a}$$

$$J = G = \frac{1}{E}\left(K_I^2 + K_{II}^2\right) + \frac{\pi}{3E}\left[K_1^2 + K_2^2 + K_3^2\frac{8(1+\nu)}{5}\right] \quad \text{for Reissner theory} \tag{25b}$$

To calculate SIF for a particular mode of loading in cases of mixed-mode loadings, we follow the scheme which was derived in [41,44] for two- or three-dimensional problems. Consider two states of a cracked model corresponding to the present state $\left(\sigma_{ij}^{(1)}, \varepsilon_{ij}^{(1)}, u_i^{(1)}\right)$ and an auxiliary stage $\left(\sigma_{ij}^{(2)}, \varepsilon_{ij}^{(2)}, u_i^{(2)}\right)$ which will be chosen as the asymptotic fields given in the Appendix. From Eq. (22), the domain form of the J-integral for the superposition of the two states is

$$\begin{aligned} J^{(1+2)} = \frac{1}{h}\int_V \Bigg(& \left(\sigma_{ij}^{(1)} + \sigma_{ij}^{(2)}\right)\frac{\partial\left(u_i^{(1)} + u_i^{(2)}\right)}{\partial x_1} \\ & - \frac{1}{2}\left(\sigma_{ij}^{(1)} + \sigma_{ij}^{(2)}\right)\left(\varepsilon_{ij}^{(1)} + \varepsilon_{ij}^{(2)}\right)\delta_{1j}\Bigg)\frac{\partial q}{\partial x_j}\mathrm{d}V \\ & - \frac{1}{h}\int_{A_1+A_2}\left(\sigma_{i3}^{(1)} + \sigma_{i3}^{(2)}\right)\frac{\partial\left(u_i^{(1)} + u_i^{(2)}\right)}{\partial x_1} n_3 q \mathrm{d}S \end{aligned} \tag{26}$$

Expanding and arranging terms in Eq. (26) gives

$$J^{(1+2)} = J^{(1)} + J^{(2)} + I^{(1,2)} \tag{27}$$

in which $I^{(1,2)}$, the so-called interaction integral, is

$$\begin{aligned} I^{(1,2)} = & \frac{1}{h}\int_V \left(\sigma_{ij}^{(1)}\frac{\partial u_i^{(2)}}{\partial x_1} + \sigma_{ij}^{(2)}\frac{\partial u_i^{(1)}}{\partial x_1} - \sigma_{ij}^{(1)}\varepsilon_{ij}^{(2)}\delta_{1j}\right)\frac{\partial q}{\partial x_j}\mathrm{d}V - \frac{1}{h} \\ & \times \int_{A_1+A_2}\left(\sigma_{ij}^{(1)}\frac{\partial u_i^{(2)}}{\partial x_1} + \sigma_{ij}^{(2)}\frac{\partial u_i^{(1)}}{\partial x_1}\right) n_3 q \mathrm{d}S \end{aligned} \tag{28}$$

Using Eq. (25), the J-integral for the combination of the present and auxiliary states is

For Kirchhoff theory,

$$\begin{aligned} J^{(1+2)} = & J^{(1)} + J^{(2)} + \frac{2}{E}\left(K_I^{(1)}K_I^{(2)} + K_{II}^{(1)}K_{II}^{(2)}\right) \\ & + \frac{2\pi}{3E}\left(\frac{1+\nu}{3+\nu}\right)\left(k_1^{(1)}k_1^{(2)} + k_2^{(1)}k_2^{(2)}\right) \end{aligned} \tag{29a}$$

For Reissner theory,

$$\begin{aligned} J^{(1+2)} = & J^{(1)} + J^{(2)} + \frac{2}{E}\left(K_I^{(1)}K_I^{(2)} + K_{II}^{(1)}K_{II}^{(2)}\right) \\ & + \frac{2\pi}{3E}\left[K_1^{(1)}K_1^{(2)} + K_2^{(1)}K_2^{(2)} + K_3^{(1)}K_3^{(2)}\frac{8(1+\nu)}{5}\right] \end{aligned} \tag{29b}$$

From Eqs. (27) and (29), we have the following relationship between the interaction integral $I^{(1,2)}$ in Eq. (28) and the SIFs

For Kirchhoff theory,

$$I^{(1,2)} = \frac{2}{E}\left(K_I^{(1)}K_I^{(2)} + K_{II}^{(1)}K_{II}^{(2)}\right) + \frac{2\pi}{3E}\left(\frac{1+\nu}{3+\nu}\right)\left(k_1^{(1)}k_1^{(2)} + k_2^{(1)}k_2^{(2)}\right) \tag{30a}$$

For Reissner theory,

$$\begin{aligned} I^{(1,2)} = & \frac{2}{E}\left(K_I^{(1)}K_I^{(2)} + K_{II}^{(1)}K_{II}^{(2)}\right) \\ & + \frac{2\pi}{3E}\left[K_1^{(1)}K_1^{(2)} + K_2^{(1)}K_2^{(2)} + K_3^{(1)}K_3^{(2)}\frac{8(1+\nu)}{5}\right] \end{aligned} \tag{30b}$$

By choosing the auxiliary state as the pure symmetric membrane loading, meaning that the asymptotic fields have only $K_I^{(2)} = 1$ and the other SIFs are equal to zero, the stress intensity factor $K_I^{(1)}$ for the present state in terms of the interactive integral $I^{(1,K_I)}$ is given as

$$K_I^{(1)} = \frac{E}{2}I^{(1,K_I)} \tag{31}$$

Similarly, we can determine the other stress intensity factors.

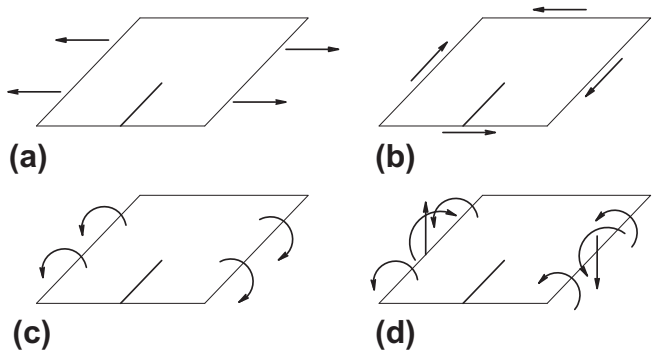

Fig. 9. Stress intensity factors related to each mode of loading; (a) Symmetric membrane loading, K_I; (b) Antisymmetric membrane loading, K_{II}; (c) Symmetric bending: Kirchhoff theory, k_1, Reissner theory, K_1; (d) Antisymmetric bending and shear: Kirchhoff theory, k_2, Reissner theory, K_2, K_3 [2].

5. Numerical examples

To verify the theory and numerical implementation described in the preceding sections, the calculation of J-integral or stress intensity factors are illustrated below in several numerical examples. Problems of plane stress and bending plate are first presented as simplified

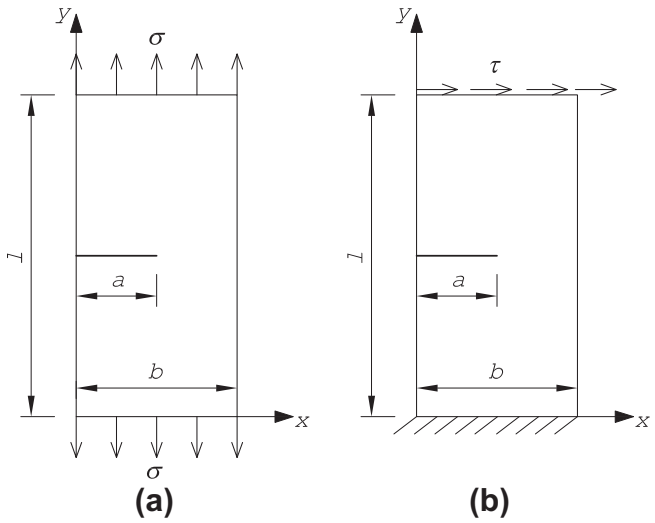

Fig. 10. Geometry of edge cracked plates under: (a) the tension, (b) the shear. The dimensions are $b = 7, a = 3.5$, and $l = 16$.

Table 1
Normalized K_I of the tension case for various meshes and integral domain sizes.

Method	Phantom-node			XFEM		
r_d/h_{avg}	mesh1	mesh2	mesh3	mesh1	mesh2	mesh3
1.5	0.872	0.953	0.959	1.045	0.972	0.958
2.0	0.882	0.953	0.960	1.104	1.006	0.991
2.5	0.878	0.953	0.960	1.114	1.002	0.988
3.0	0.879	0.953	0.961	1.113	1.003	0.989

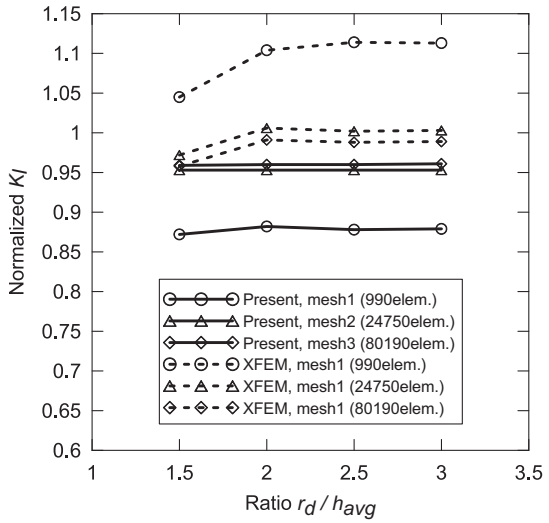

Fig. 11. Normalized K_I for the edge cracked plate under tension with different meshes and J-integral domain sizes: phantom-node method (continuous lines) and XFEM (dash lines).

cases of typical shell models. Subsequently, examples of circular cylinders with different directions of crack are considered.

5.1. Edge cracked plates under tension or shear

Consider a plane stress plate of width $b = 7$, height $l = 16$, and thickness $h = 1$ with an edge crack length of $a = b/2$. The material properties are $E = 3 \times 10^7$, and $\nu = 0.25$. The plate is subjected to a tension $\sigma = 1$ at the top and bottom edges as shown in Fig. 10a, or is clamped onto the bottom edge and sustains a shear $\tau = 1$ on the top edge (see Fig. 10b).

Table 2
Normalized K_I of the shear case for various meshes and integral domain sizes.

Method	Phantom-node			XFEM		
r_d/h_{avg}	mesh1	mesh2	mesh3	mesh1	mesh2	mesh3
1.5	0.799	0.962	0.986	0.989	0.986	0.984
2.0	0.812	0.967	0.985	1.039	1.021	1.021
2.5	0.808	0.966	0.984	1.047	1.019	1.017
3.0	0.809	0.966	0.985	1.046	1.019	1.018

Table 3
Normalized K_{II} of the shear case for various meshes and integral domain sizes.

Method	Phantom-node			XFEM		
r_d/h_{avg}	mesh1	mesh2	mesh3	mesh1	mesh2	mesh3
1.5	0.803	1.004	1.051	0.653	0.990	1.104
2.0	0.827	0.975	1.031	0.901	1.000	1.034
2.5	0.846	0.977	1.014	0.886	0.985	1.012
3.0	0.847	0.979	1.013	0.898	0.988	1.013

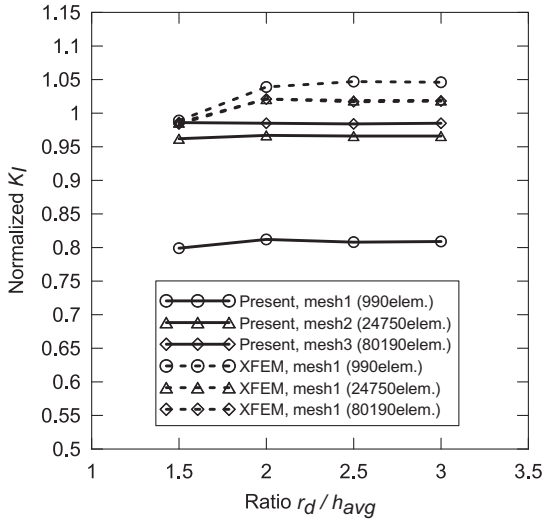

Fig. 12. Normalized K_I for the edge cracked plate under shear with different meshes and J-integral domain sizes: phantom-node method (continuous lines) and XFEM (dash lines).

The analytical solution for the plate under tension is given in [41]

$$K_I = C\sigma\sqrt{\pi a} \tag{32}$$

with $C = 1.12 - 0.231(a/b) + 10.55(a/b)^2 - 21.72(a/b)^3 - 30.39(a/b)^4$

The values of K_I and K_{II} for the shear case in [45] are used as the reference solutions:

$$K_I = 34.0, \quad K_{II} = 4.55 \tag{33}$$

The plate is modeled by various structured meshes ($n_x \times n_y$) defined as the number of elements along the x and y axes (see Fig. 10), respectively. These are three structured meshes of (15×32), (75×165), and (135×297) MITC3 shell elements. In the following tables and figures, these meshes are denoted as mesh1, mesh2, and mesh3. The numerical results normalized by the reference solutions are given in Table 1 and Fig. 11 for the tension, and Tables 2 and 3 and Figs. 12 and 13 for the shear. The structure mesh and displacement fields are illustrated in Fig. 14.

The results show that as mesh density increases the stress intensity factors approach the reference solutions and are mostly

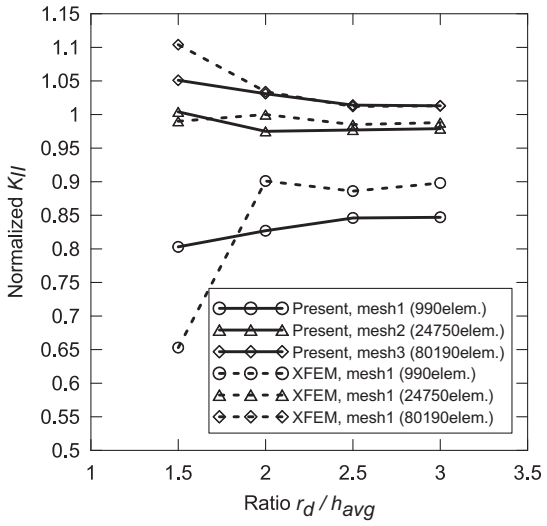

Fig. 13. Normalized K_{II} for the edge cracked plate under shear with different meshes and J-integral domain sizes: phantom-node method (continuous lines) and XFEM (dash lines).

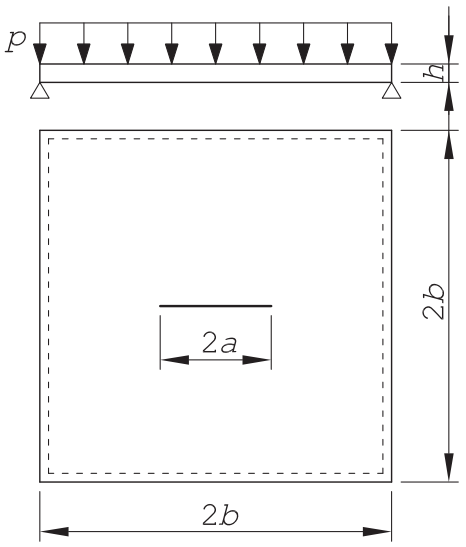

Fig. 15. Dimensions of a central cracked plate (simply supported all around) subjected to uniform pressure.

independent of the domain sizes of the interaction integral. Reasonable values of r_d/h_{avg} range from 2.0 to 3.0, where r_d and h_{avg} were defined in Section 4.1. We also present the SIFs computed by the XFEM using three-node triangular elements with the asymptotic enrichment functions at the tip elements in the plane stress condition [46]. Compared to the XFEM, the phantom-node method requires fine mesh to obtain acceptable results. However, the asymptotic enrichment functions are known for this type of problem. For other more complex problems where the solution is not known, asymptotic enrichment does not necessarily provide more accurate results but introduces additional complexity and parameters that need to be calibrated.

5.2. Central cracked plates under pressure

This example considers a square plate with a central crack subjected to uniform pressure $p = 1.0$. The plate is simply supported on all edges. The geometry shows $b = 1.0$ in Fig. 15. Material properties are $E = 1000$, and $\nu = 0.3$.

The plate is discretized by a regular mesh of (81×81) MITC3 shell elements. Three different domain sizes were used to verify the path-independence of the J-integral and meshing quality for the case where $b/h = 10$. The values of J-integral are given in Table 4. The difference between the J values on the domain sizes

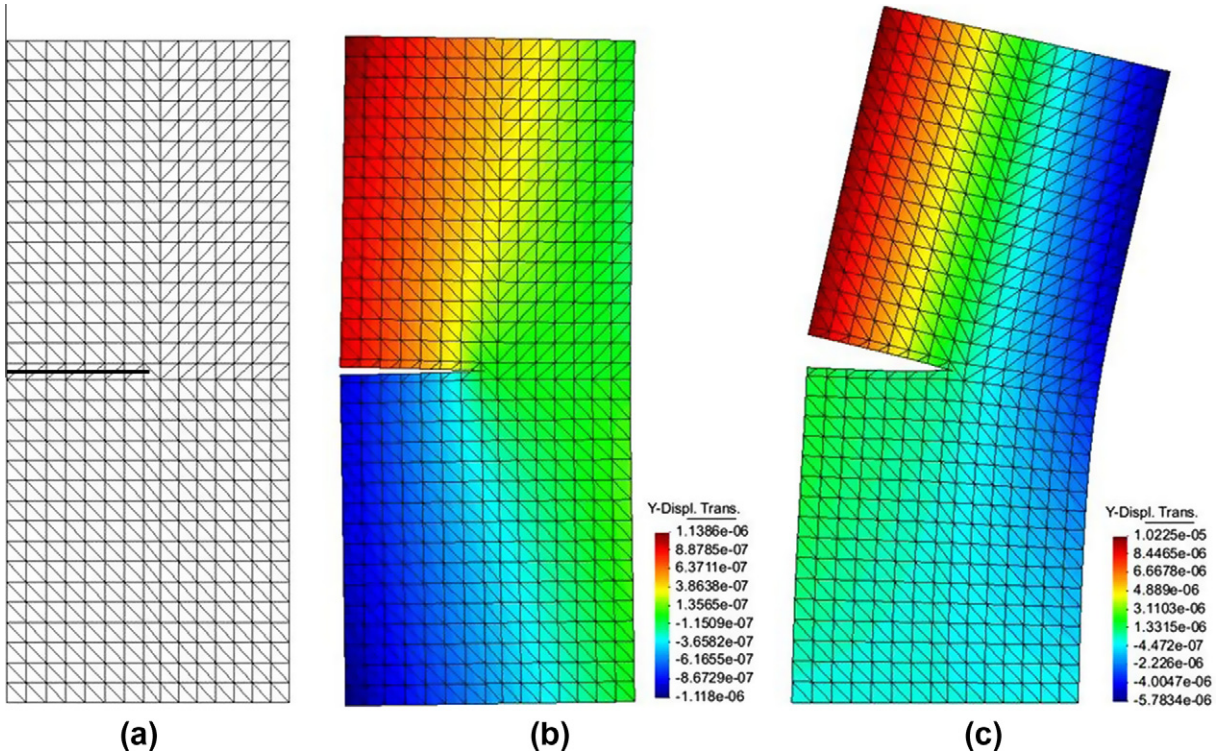

Fig. 14. (a) Structured mesh with (15×32) MITC3 shell elements for the edge cracked plate; Vertical displacement field: (b) under the tension, (c) under the shear. The deformation factor is 10^5.

Table 4
J-integral in cases of various crack lengths and domain sizes, $b/h = 10$.

r_d/h_{avg}	a/b								
	0.1	0.2	0.3	0.4	0.5	0.6	0.7	0.8	0.9
1.5	0.738	1.265	1.672	1.938	2.036	1.947	1.668	1.216	0.640
2.5	0.731	1.260	1.665	1.922	2.006	1.897	1.591	1.106	0.494
3.5	0.687	1.196	1.578	1.812	1.872	1.738	1.408	0.899	0.267

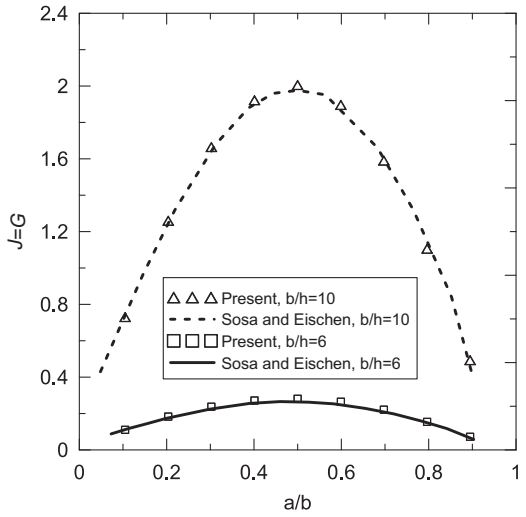

Fig. 16. *J*-integral values of the central cracked plate (simply supported all around) subjected to uniform pressure.

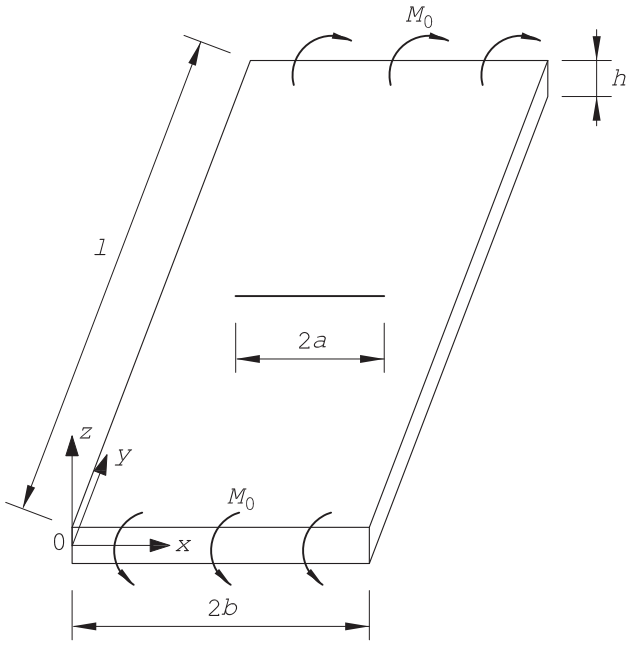

Fig. 17. Geometry of a central cracked plate under a uniform far-field moment.

significantly occurs in cases of the tips near the boundary, meaning that a denser mesh should be used.

Results of the *J*-integral for various lengths of the central crack in two different cases of thickness, $b/h = 6$ and $b/h = 10$, are illustrated in Fig. 16. Because of the boundary constraints, the *J*-integral, or the energy release rate *G*, decreases as the tips of the crack approach the edges. The results accord well with those solved by Sosa and Eischen [47] using the finite element method and a path-independent *J*-integral. Notice that the problem under consideration has only the symmetric bending mode.

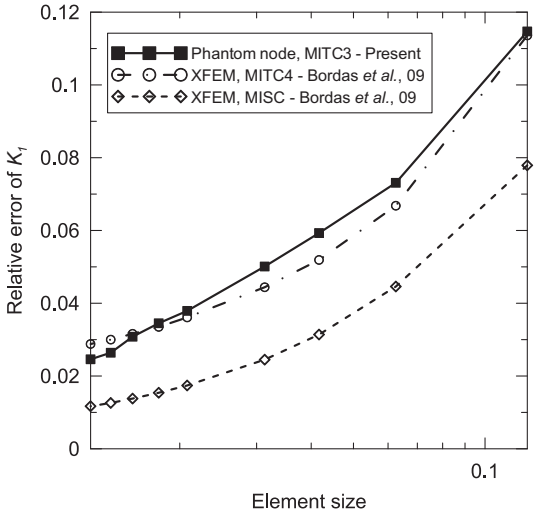

Fig. 18. Convergence of relative error in K_1 of a central cracked plate subjected to a uniform far-field moment.

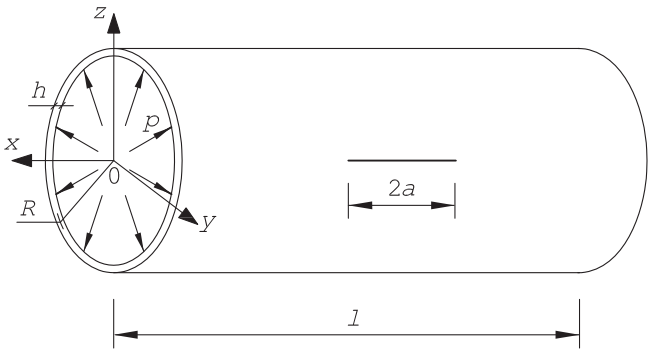

Fig. 19. Geometry of a cylinder with an axial crack under internal pressure.

5.3. Central cracked plate under a uniform far-field moment

To compare the SIF convergence given by the present method and the XFEM we consider a benchmark problem which is a rectangular plate containing a through-the-thickness crack and subjected to a uniform far-field moment. Under such boundary conditions, the plate is loaded by a purely mode *I* stress intensity factor of symmetric bending. Analytical calculations were studied by Boduroglu and Erdogan using Reissner's transverse shear theory.

Following the paper of Bordas et al. the plate dimensions are taken to be a width of $2b = 2$, a length of $l = 6$ and a thickness of $h = b/4$. The length of the crack is $2a = 1.0$. A constant distributed moment of $M_0 = 1$ is applied on both edges of the plate parallel to the crack, as shown in Fig. 17. The material is isotropic elasticity with a Young's modulus of $E = 200$GPa and Poisson's ratio of $\nu = 0.3$.

The SIF of symmetric bending, K_1, is numerically solved using various regular meshes of MITC3 shell elements which differ in the size of the edges. Compared to the analytical solution given in ,the convergence of relative error in K_1 with respect to element size is illustrated in Fig. 18. The figure also shows the convergence

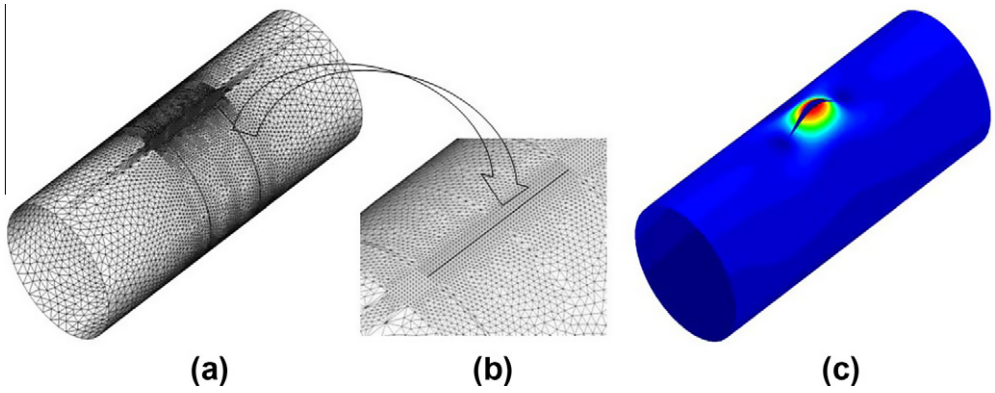

Fig. 20. (a) Typical mesh of a cylinder with an axial crack; (b) Regular and fine mesh near the crack; (c) Displacement field with crack opening (Deformation factor 0.05).

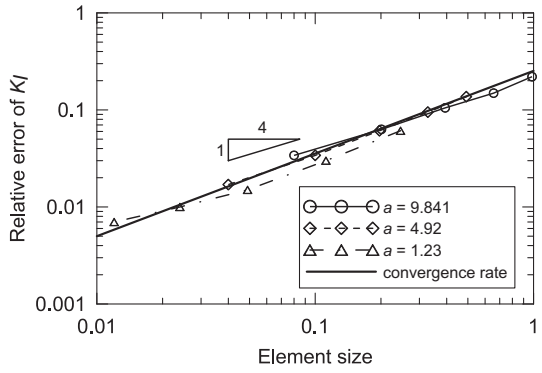

Fig. 21. Relative errors of the K_I vs. element size obtained by the phantom-node method. The continuous bold line shows the optimal convergence rate, which is about 1/4.

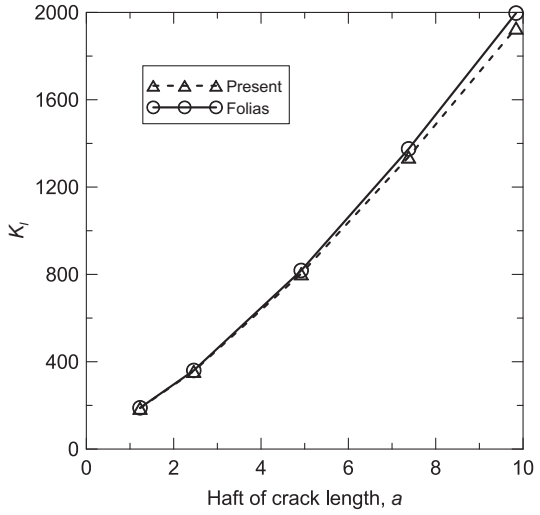

Fig. 22. Stress intensity factor K_I corresponding to membrane symmetric loading.

computed by Bordas et al. using the XFEM which incorporates tip enrichments into the formulation of MITC4 [37] or MISC plate elements. The XFEM employing the enriched MISC elements gives superior convergence over the present method because the smoothing curvature of the plate elements improves the accuracy of the MITC elements. However, the convergence rates of the present method which ignores tip enrichments and the XFEM using the enriched MITC4 are similar, especially in the cases of very fine meshes. The slight difference may be due to the greater accuracy of the MITC4 than the MITC3 elements. Therefore, tip enrichments are not necessary for plates or shells.

5.4. Pressurized cylinder with an axial crack

A thin walled cylinder with the mean radius $R = 20$, thickness $h = 0.25$, and length $l = 100$ containing an axial through-the-thickness crack of length $2a$ is subjected to an internal pressure $p = 1.0$ (see Fig. 19). E is 1000, and $\nu = 0.3$. We support open-end conditions.

Table 5
J-integral of circumferentially cracked cylinder under tension.

2γ	R/h	Present	Ref. [49]	Ref. [50]	Ref. [48]
45°	40	3.03×10^{-2}	3.24×10^{-2}	3.09×10^{-2}	
	6.2	4.10×10^{-4}	4.56×10^{-4}		4.23×10^{-4}
90°	20	2.40×10^{-2}	2.57×10^{-2}	2.48×10^{-2}	

The mesh used for calculations is regular and fine around the crack area but irregular and gradually coarse in the other area remote from the crack. The typical mesh and displacement field

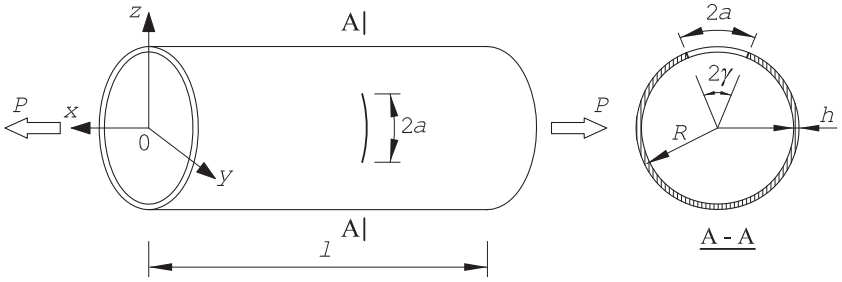

Fig. 23. Geometry of a cylinder with a circumferential crack under tension.

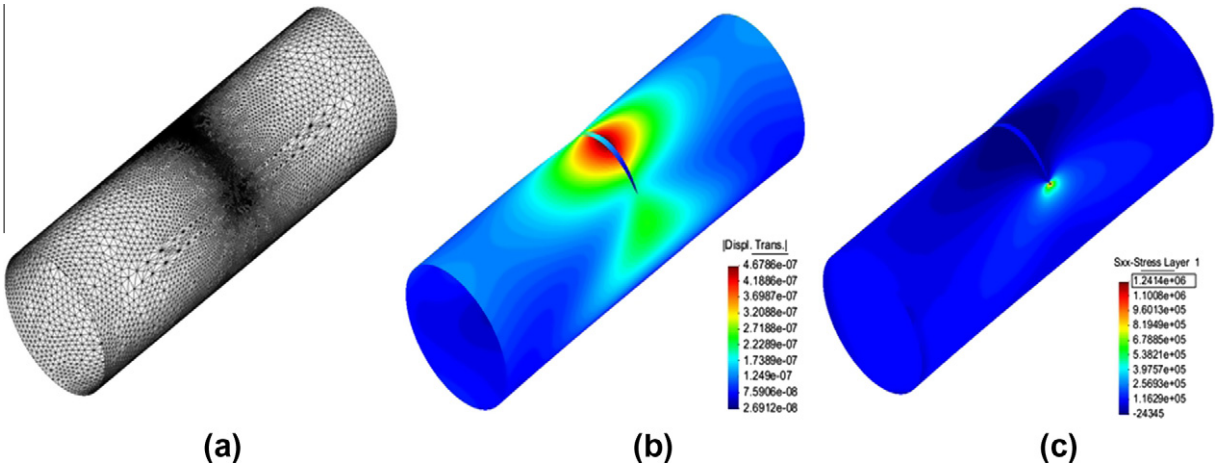

Fig. 24. Cylinder containing a circumferential crack with an angle 90° under tension: (a) meshing; (b) displacement field; (c) normal stress field in the tension direction (Deformation factor 2×10^4).

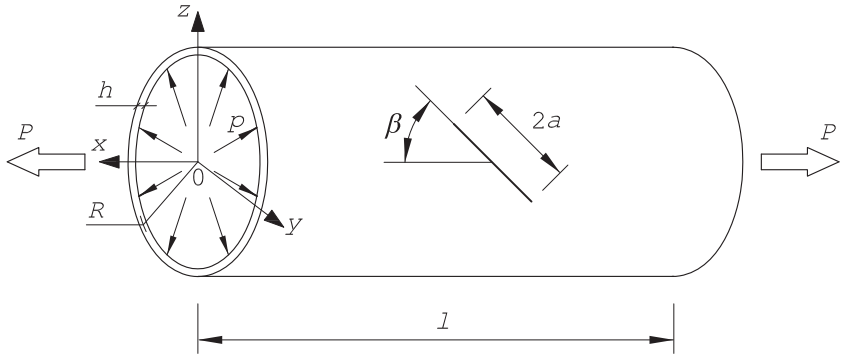

Fig. 25. Geometry of a cylinder with a crack inclined at an angle β under uniform internal pressure.

with crack opening are depicted in Fig. 20 for the cylinder with a crack length of $2a = 19.682$.

The interaction integral I for the Kirchhoff theory is employed to extract the stress intensity factor K_I of symmetric membrane loading. Because the stress intensity factor is mostly influenced by the stress and strain fields near the crack tip, various regular meshes around the crack, which differ in the length of triangular elements, are placed to investigate the dependence of accuracy on the meshes. Fig. 21 presents the relationship between the length of elements in the regular meshes around the crack and the relative error of K_I which is obtained based on the analytical solution given by Folias [48]. In this figure, the convergence rate of K_I is about 1/4 and K_I can be calculated within 4% accuracy using triangular elements of length $a/123$.

Fig. 22 shows the values of K_I for various axial cracks of lengths $2a = 2.46$, 4.92, 9.84, 14.76 or 19.682. In all the cases, elements of length $a/123$ are used for structured mesh around the crack. These results are in good agreement with the analytical solution of Folias [48].

Table 6
J values of a pressurized cylinder with variously inclined cracks.

R/h	Scale	β (degree)				
		0	30	45	60	90
6.2	$\times 10^{-10}$	39.4	29.2	21.0	13.3	5.5
20	$\times 10^{-9}$	91.7	64.3	44.1	26.6	8.7
40	$\times 10^{-8}$	62.7	42.9	29.6	18.1	4.8

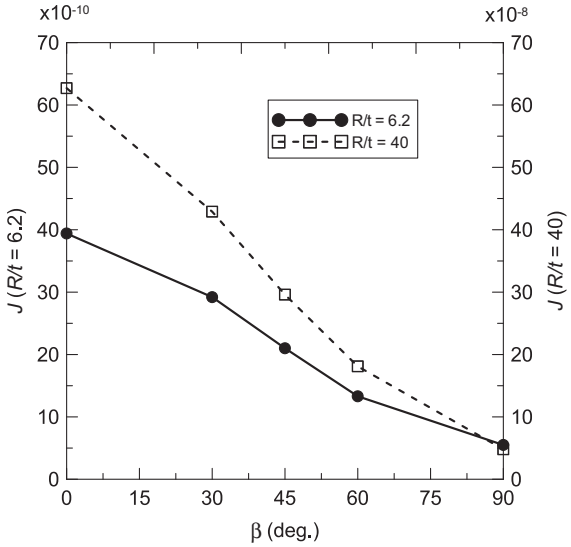

Fig. 26. J value vs. angle β for a pressurized cylinder with an inclined crack. The left axis is for $R/h = 6.2$. The right axis is for $R/h = 40$.

5.5. Cylinder with a circumferential crack under tension

We compute here the J value of a cylinder with radius $R = 0.0529$ and thickness h containing a circumferential

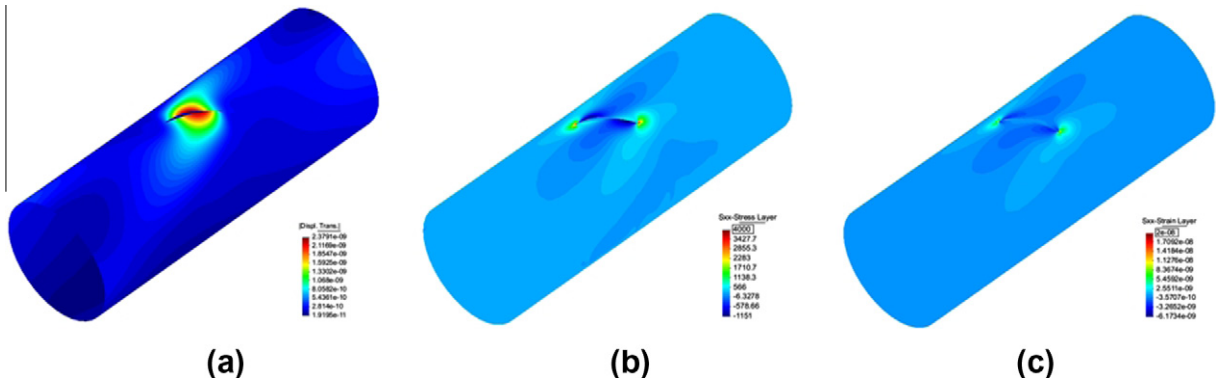

Fig. 27. A pressurized cylinder ($R/h = 40$) with a crack inclined at an angle: (a) $\beta = 30°$: displacement; (b) $\beta = 45°$: stress σ_{xx}; (c) $\beta = 60°$: strain ε_{xx} (Deformation factor 2×10^6).

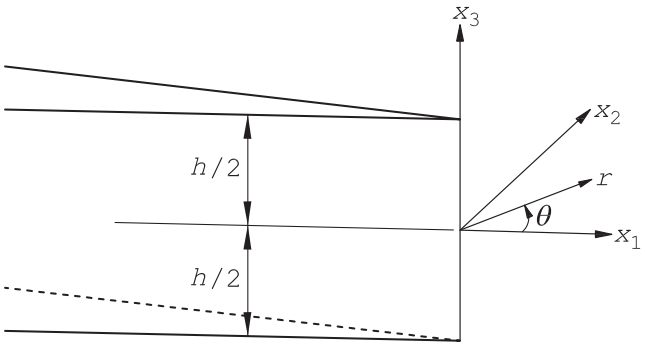

Fig. 28. Local coordinates at the tip of a crack in a shell model.

through-wall crack of length $2a = 2\gamma R$ in the circular direction, where 2γ is the total included angle (see Fig. 23). Tensile forces $P = 90$ are applied on both ends of the cylinder. Material properties are $E = 2.07 \times 10^{11}$ and $\nu = 0.3$. This example was solved by LePort et al. [49] using the finite element method and virtual crack extension method for energy release rate calculation.

Table 5 presents J values obtained by the phantom-node method and the domain form of the J-integral in various cases of the crack length and shell thickness. The results are similar to those calculated by [49] and the analytical solutions given in [48,50]. The crack opening is shown in Fig. 24 as well as the displacement field and concentration of tension stress near the crack tips.

5.6. Pressurized cylinder with an inclined crack

Consider the cylinder given in Section 5.5 but containing a crack of length $2a = 0.05$ inclined an angle of β as shown in Fig. 25. The cylinder is subjected to a uniform internal pressure $p = 10$ and an axial extension $P = 8.8 \times 10^{-2}$. This load condition is equivalent to the cylinder with both end caps under the internal pressure $p = 10$.

Table 6 presents calculated J values for the cylinder with the crack inclined different angles of β and various thicknesses of the cylinder. When the thickness decreases, the J value or the energy release rate G increases. Fig. 26 demonstrates the decrease of J values as the crack changes from the axial to perpendicular direction with respect to the cylindrical axis in the cases of thickness $R/h = 6.2$ and 40. To the knowledge of the authors, no results are available that can be compared with our results, and these results can thus be used as a reference. The distributions of displacement, stress and strain fields with crack opening are illustrated in Fig. 27 for the case $R/h = 40$.

6. Conclusions

The phantom-node method has been developed for shell models discretized by MITC3 elements. The method is useful for the smooth growth of a crack since it permits crack tips to be arbitrarily located within an element. Since discontinuity across the crack is described using continuities constructed from full interpolation bases of overlapping paired elements, the separate interpolation of transverse shear strains (MITC technique) can be employed straightforwardly. Therefore, the presented method allows the modeling of both thin and thick shell structures with the crack independent of the finite element mesh.

The equivalent domain integral technique applied for three-dimensional problems has been derived for shell models using continuum mechanics based shell elements to compute the J-integral, or the energy release rate. Extraction of stress intensity factors was also formulated based on the interaction integral. The domain form of integrals can be easily implemented in the context of the phantom-node method as a post-processing stage. Due to the MITC3 used, the methodology in this paper has computed the fracture parameters for both thin and thick shells.

Several numerical examples, i.e. plane stress, plate, and shell problems containing cracks have been studied to demonstrate the efficiency of the present method. Working as the finite element method without the quarter point elements at the crack tips, the mesh of finite element should be fine enough in areas surrounding the crack tips to obtain accuracy of calculation. In the examples, numerical results are in excellent agreement with the analytical solutions or those given in the references.

Acknowledgments

Authors Thanh Chau-Dinh and Goangseup Zi would like to thank the Agency for Defense Development (ADD) for their Grants UD090012JD and Basic Science Research Program through the National Research Foundation of Korea (NRF) funded by the Ministry of Education, Science and Technology (2011-0003166). Author Timon Rabczuk is grateful for the support provided by the German Research Foundation (DFG).

Appendix A. Asymptotic fields near a crack tip

The stress and displacement fields with respect to a polar coordinate system (r, θ) at a crack tip shown in Fig. 28 are given as follows [2].

For membrane loading:

$$\begin{Bmatrix}\sigma_{11}\\ \sigma_{12}\\ \sigma_{22}\end{Bmatrix}=\frac{K_I}{\sqrt{2\pi r}}\cos\frac{\theta}{2}\begin{Bmatrix}1-\sin\frac{\theta}{2}\sin\frac{3\theta}{2}\\ \sin\frac{\theta}{2}\cos\frac{3\theta}{2}\\ 1+\sin\frac{\theta}{2}\sin\frac{3\theta}{2}\end{Bmatrix}+\frac{K_{II}}{\sqrt{2\pi r}}\begin{Bmatrix}-\sin\frac{\theta}{2}\left(2+\cos\frac{\theta}{2}\cos\frac{3\theta}{2}\right)\\ \cos\frac{\theta}{2}\left(1-\sin\frac{\theta}{2}\sin\frac{3\theta}{2}\right)\\ \sin\frac{\theta}{2}\cos\frac{\theta}{2}\cos\frac{3\theta}{2}\end{Bmatrix} \tag{A.1}$$

and

$$\begin{Bmatrix}u_1\\ u_2\end{Bmatrix}=\frac{K_I}{2\mu}\sqrt{\frac{r}{2\pi}}\begin{Bmatrix}\cos\frac{\theta}{2}\left(2\frac{1-\nu}{1+\nu}+2\sin^2\frac{\theta}{2}\right)\\ \sin\frac{\theta}{2}\left(\frac{4}{1+\nu}-2\cos^2\frac{\theta}{2}\right)\end{Bmatrix}+\frac{K_{II}}{2\mu}\sqrt{\frac{r}{2\pi}}\begin{Bmatrix}\sin\frac{\theta}{2}\left(\frac{4}{1+\nu}+2\cos^2\frac{\theta}{2}\right)\\ -\cos\frac{\theta}{2}\left(2\frac{1-\nu}{1+\nu}-2\sin^2\frac{\theta}{2}\right)\end{Bmatrix} \tag{A.2}$$

where $\mu = E/2(1+\nu)$ is the shear modulus.

For bending and transverse shear loading in the context of Kirchhoff theory:

$$\begin{Bmatrix}\sigma_{rr}\\ \sigma_{r\theta}\\ \sigma_{\theta\theta}\end{Bmatrix}=\frac{k_1}{\sqrt{2r}}\frac{x_3}{2h}\frac{1}{3+\nu}\begin{Bmatrix}(3+5\nu)\cos\frac{\theta}{2}-(7+\nu)\cos\frac{3\theta}{2}\\ -(1-\nu)\sin\frac{\theta}{2}+(7+\nu)\sin\frac{3\theta}{2}\\ (5+3\nu)\cos\frac{\theta}{2}+(7+\nu)\cos\frac{3\theta}{2}\end{Bmatrix}+\frac{k_2}{\sqrt{2r}}\frac{x_3}{2h}\frac{1}{3+\nu}\begin{Bmatrix}-(3+5\nu)\sin\frac{\theta}{2}+(5+3\nu)\sin\frac{3\theta}{2}\\ (-1+\nu)\cos\frac{\theta}{2}+(5+3\nu)\cos\frac{3\theta}{2}\\ -(5+3\nu)\left(\sin\frac{\theta}{2}+\sin\frac{3\theta}{2}\right)\end{Bmatrix} \tag{A.3}$$

$$\begin{Bmatrix}\sigma_{r3}\\ \sigma_{\theta3}\end{Bmatrix}=\frac{1}{(2r)^{\frac{3}{2}}}\frac{1}{3+\nu}\frac{h}{2}\left[1-\left(\frac{2x_3}{h}\right)^2\right]\begin{Bmatrix}-k_1\cos\frac{\theta}{2}+k_2\sin\frac{\theta}{2}\\ -k_1\sin\frac{\theta}{2}-k_2\cos\frac{\theta}{2}\end{Bmatrix} \tag{A.4}$$

$$\sigma_{33}=0 \tag{A.5}$$

and

$$u_3=\frac{(2r)^{\frac{3}{2}}(1-\nu^2)}{2Eh(3+\nu)}\left\{k_1\left[\frac{1}{3}\left(\frac{7+\nu}{1-\nu}\right)\cos\frac{3\theta}{2}-\cos\frac{\theta}{2}\right]+k_2\left[-\frac{1}{3}\left(\frac{5+3\nu}{1-\nu}\right)\sin\frac{3\theta}{2}+\sin\frac{\theta}{2}\right]\right\} \tag{A.6}$$

For bending and transverse shear loading in the context of Reissner theory:

$$\begin{Bmatrix}\sigma_{rr}\\ \sigma_{r\theta}\\ \sigma_{\theta\theta}\end{Bmatrix}=\frac{K_1}{\sqrt{2r}}\frac{x_3}{2h}\begin{Bmatrix}5\cos\frac{\theta}{2}-\cos\frac{3\theta}{2}\\ \sin\frac{\theta}{2}+\sin\frac{3\theta}{2}\\ 3\cos\frac{\theta}{2}+\cos\frac{3\theta}{2}\end{Bmatrix}+\frac{K_2}{\sqrt{2r}}\frac{x_3}{2h}\begin{Bmatrix}-5\sin\frac{\theta}{2}+3\sin\frac{3\theta}{2}\\ \cos\frac{\theta}{2}+3\cos\frac{3\theta}{2}\\ -3\sin\frac{\theta}{2}-3\sin\frac{3\theta}{2}\end{Bmatrix} \tag{A.7}$$

$$\begin{Bmatrix}\sigma_{r3}\\ \sigma_{\theta3}\end{Bmatrix}=\frac{K_3}{\sqrt{2r}}\left[1-\left(\frac{2x_3}{h}\right)^2\right]\begin{Bmatrix}\sin\frac{\theta}{2}\\ \cos\frac{\theta}{2}\end{Bmatrix} \tag{A.8}$$

and

$$u_3=\frac{\sqrt{2}r^{\frac{3}{2}}(1-\nu)}{Eh}\left\{K_1\left[\frac{1}{3}\left(\frac{7+\nu}{1-\nu}\right)\cos\frac{3\theta}{2}-\cos\frac{\theta}{2}\right]+K_2\left[-\frac{1}{3}\left(\frac{5+3\nu}{1-\nu}\right)\sin\frac{3\theta}{2}+\sin\frac{\theta}{2}\right]\right\}+\frac{8\sqrt{2r}(1+\nu)}{5E}K_3\sin\frac{\theta}{2} \tag{A.9}$$

$$\chi=\frac{5r^{\frac{3}{2}}}{3\sqrt{2}(1+\nu)}\left[K_1\left(\sin\frac{3\theta}{2}+\sin\frac{\theta}{2}\right)+K_2\left(\frac{1}{3}\cos\frac{3\theta}{2}+\cos\frac{\theta}{2}\right)\right]-\frac{2\sqrt{2r}h}{3}K_3\cos\frac{\theta}{2} \tag{A.10}$$

The scalar function χ is related to the transverse shear resultants by

$$Q_{13}=\frac{\partial\chi}{\partial x_2},\quad Q_{23}=-\frac{\partial\chi}{\partial x_1} \tag{A.11}$$

and is further used in the equations for the in-plane displacements

$$u_\alpha=-x_3\frac{\partial w(x_1,x_2)}{\partial x_\alpha}+\frac{12(1+\nu)}{5Eh}x_3Q_{\alpha3}(x_1,x_2) \tag{A.12}$$

where $\alpha = 1, 2$.

References

[1] Lemaitre J, Turbat A, Loubet R. Fracture mechanics analysis of pressurized cracked shallow shells. Eng Fract Mech 1977;9:443–60.
[2] Zehnder AT, Viz MJ. Fracture mechanics of thin plates and shells under combined membrane, bending, and twisting loads. Appl Mech Rev ASME 2005;58:37–48.
[3] Barsoum RS, Loomis RW, Stewart BD. Analysis of through cracks in cylindrical shells by the quarter-point elements. Int J Fract 1979;15:259–80.
[4] Potyondy DO, Wawrzynek PA, Ingraffea AR. An algorithm to generate quadrilateral or triangular element surface meshes in arbitrary domains with applications to crack propagation. Int J Numer Methods Eng 1995;38:2677–701.
[5] Nguyen-Dang H, Tran TN. Analysis of cracked plates and shells using metis finite element model. Finite Elem Anal Des 2004;40:855–78.
[6] Furukawa CH, Bucalem ML, Mazella IJG. On the finite element modeling of fatigue crack growth in pressurized cylindrical shells. Int J Fract 2009;31:629–35.
[7] Rabczuk T, Areias PMA. A meshfree thin shell for arbitrary evolving cracks based on an extrinsic basis. Comput Model Eng Sci 2006;16:115–30.
[8] Rabczuk T, Areias PMA, Belytschko T. A meshfree thin shell method for non-linear dynamic fracture. Int J Numer Methods Eng 2007;72:524–48.
[9] Rabczuk T, Gracie R, Song JH, Belytschko T. Immersed particle method for fluid–structure interaction. Int J Numer Methods Eng 2010;81:48–71.
[10] Areias PMA, Belytschko T. Non-linear analysis of shells with arbitrary evolving cracks using XFEM. Int J Numer Methods Eng 2005;62:384–415.
[11] Nagashima T, Suemasu H. X-FEM analysis of a thin-walled composite shell structure with a delamination. Comput Struct 2010;88:549–57.
[12] Larsson R, Mediavilla J, Fagerström M. Dynamic fracture modeling in shell structures based on XFEM. Int J Numer Methods Eng 2011;86:499–527.
[13] Dvorkin EN, Bathe KJ. A continuum mechanics based four-node shell element for general non-linear analysis. Eng Comput 1984;1:77–88.
[14] Andelfinger U, Ramm E. EAS-elements for two-dimensional, three-dimensional, plate and shell structures and their equivalence to HR-elements. Int J Numer Methods Eng 1993;36:1311–37.
[15] Nguyen-Thanh N, Rabczuk T, Nguyen-Xuan H, Bordas S. A smoothed finite element method for shell analysis. Comput Methods Appl Mech Eng 2008;198:165–77.
[16] Hansbo A, Hansbo P. A finite element method for the simulation of strong and weak discontinuities in solid mechanics. Comput Methods Appl Mech Eng 2004;193:3523–40.
[17] Areias PMA, Belytschko T, A comment on the article. In: Hansbo A, Hansbo P, editor. A finite element method for simulation of strong and weak discontinuities in solid mechanics [Comput. Methods Appl. Mech. Engrg. 193 (2004) 3523–40], Computer Methods in Applied Mechanics and Engineering 195 2006. p. 1275–76.
[18] Mergheim J, Kuhl E, Steinmann P. A finite element method for the computational modelling of cohesive cracks. Int J Numer Methods Eng 2005;63:276–89.
[19] Rabczuk T, Zi G, Gerstenberger A, Wall WA. A new crack tip element for the phantom-node method with arbitrary cohesive cracks. Int J Numer Methods Eng 2008;75:577–99.
[20] Mergheim J, Kuhl E, Steinmann P. Towards the algorithmic treatment of 3D strong discontinuities. Commun Numer Methods Eng 2007;23:97–108.
[21] Duan Q, Song JH, Menouillard T, Belytschko T. Element-local level set method for three-dimensional dynamic crack growth. Int J Numer Methods Eng 2009;80:1520–43.
[22] Areias PMA, Song JH, Belytschko T. Analysis of fracture in thin shells by overlapping paired elements. Comput Methods Appl Mech Eng 2006;195:5343–60.
[23] Song JH, Areias PMA, Belytschko T. A method for dynamic crack and shear band propagation with phantom nodes. Int J Numer Methods Eng 2006;67:868–93.
[24] Song JH, Belytschko T. Dynamic fracture of shells subjected to impulsive loads. J Appl Mech ASME 2009;76:051301–1–9.
[25] Lee PS, Bathe KJ. Development of MITC isotropic triangular shell finite elements. Comput Struct 2004;82:945–62.
[26] Lee PS, Noh HC, Bathe KJ. Insight into 3-node triangular shell finite elements: the effects of element isotropy and mesh patterns. Comput Struct 2007;85:404–18.
[27] Nikishkov GP, Atluri SN. Calculation of fracture mechanics parameters for an arbitrary three-dimensional crack, by the 'Equivalent Domain Integral' method. Int J Numer Methods Eng 1987;24:1801–21.
[28] Ahmad S, Irons BM, Zienkiewicz OC. Analysis of thick and thin shell structures by curved finite elements. Int J Numer Methods Eng 1970;2:419–51.
[29] Yang HTY, Saigal S, Masud A, Kapania RK. A survey of recent shell finite elements. Int J Numer Methods Eng 2000;47:101–27.

[30] Lee PS, Bathe KJ. On the asymptotic behavior of shell structures and the evaluation in finite element solutions. Comput Struct 2002;80:235–55.
[31] Zienkiewicz OC, Taylor RL, Too JM. Reduced integration technique in general analysis of plates and shells. Int J Numer Methods Eng 1971;3:275–90.
[32] Parisch H. A critical survey of the 9-node degenerated shell element with special emphasis on thin shell application and reduced integration. Comput Methods Appl Mech Eng 1979;20:323–50.
[33] Belytschko T, Wong BL, Chiang HY. Advances in one-point quadrature shell elements. Comput Methods Appl Mech Eng 1992;96:93–107.
[34] Belytschko T, Leviathan I. Physical stabilization of the 4-node shell element with one point quadrature. Comput Methods Appl Mech Eng 1994;113:321–50.
[35] Jang J, Pinsky PM. An assumed covariant strain based 9-node shell element. Int J Numer Methods Eng 1987;24:2389–411.
[36] Sze KY, Zhu D. A quadratic assumed natural strain curved triangular shell element. Comput Methods Appl Mech Eng 1999;174:57–71.
[37] Bathe KJ, Dvokin EN. A formulation of general shell elements—The use of mixed interpolation of tensorial components. Int J Numer Methods Eng 1986;22:697–722.
[38] Kasper EP, Taylor RL. A mixed-enhanced strain method: Part I: Geometrically linear problems. Comput Struct 2000;75:237–50.
[39] Bathe KJ, Lee PS. Measuring the convergence behavior of shell analysis schemes. Comput Struct 2011;89:285–301.
[40] Bathe KJ. Finite Element Procedures. Prentice Hall; 1996.
[41] Moës N, Dolbow J, Belytschko T. A finite element method for crack growth without remeshing. Int J Numer Methods Eng 1999;46:131–50.
[42] Dolbow J, Moës N, Belytschko T. Modeling fracture in Mindlin–Reissner with the extended finite element method. Int J Solids Struct 2000;33:7161–83.
[43] Zi G, Belytschko T. New crack-tip elements for XFEM and applications to cohesive cracks. Int J Numer Methods Eng 2003;57:2221–40.
[44] M öes N, Gravouil A, Belytschko T. Non planar 3D crack growth by the extended finite elements and the level sets. Part I: Mechanical model. Int J Numer Methods Eng 2002;53(11):2549–68.
[45] Yau JF, Wang SS, Corten HT. A mixed-mode crack analysis of isotropic solids using conservation laws of elasticity. J Appl Mech ASME 1980;47:335–41.
[46] Zi G, Song JH, Budyn E, Lee SH, Belytschko T. A method for growing multiple cracks without remeshing and its application to fatigue crack growth. Modell Simulat Aerials Sci Eng 2004;12:901–15.
[47] Sosa H, Eischen J. Computation of stress intensity factors for plate bending via a path-independent integral. Eng Fract Mech 1986;25:451–62.
[48] Folias ES. On the effect of initial curvature on cracked flat sheets. Int J Fract Mech 1969;5:327–46.
[49] LePort P, deLorenzi HG, Kumar V, German MD. Virtual crack extension method for energy release rate calculations in flawed thin shell structures. J Press Vessel Technol ASME 1987;109:101–7.
[50] Sander Jr JL. Circumferential through-cracks in cylindrical shells under tension. J Appl Mech ASME 1982;49:103–7.